Research Article | Vol. 9, No. 5 | 1 May 2018 | BIOMEDICAL OPTICS EXPRESS 2229
Biomedical Optics EXPRESS

Performance of optoacoustic and fluorescence imaging in detecting deep-seated fluorescent agents

ZHENYUE CHEN,[1] XOSÉ LUÍS DEÁN-BEN,[1] SVEN GOTTSCHALK,[1] AND DANIEL RAZANSKY[1,2,*]

[1]*Institute for Biological and Medical Imaging (IBMI), Helmholtz Center Munich, Ingolstädter Landstr. 1, 85764 Neuherberg, Germany*
[2]*Faculty of Medicine, Technical University of Munich, Ismaninger Str. 22, 81675 Munich, Germany*
**dr@tum.de*

Abstract: Fluorescent contrast agents are widely employed in biomedical research. While many studies have reported deep tissue imaging of fluorescent moieties using either fluorescence-based or absorption-based (optoacoustic) imaging systems, no systematic comparison has been performed regarding the actual performance of these imaging modalities in detecting deep-seated fluorescent agents. Herein, an integrated imager combining epi-fluorescence and volumetric optoacoustic imaging capabilities has been employed in order to evaluate image degradation with depth for several commonly-used near-infrared dyes in both modes. We performed controlled experiments in tissue-mimicking phantoms containing deeply embedded targets filled with different concentrations of Alexa Fluor 700, Alexa Fluor 750, indocyanine green (ICG) and IRDye 800CW. The results are further corroborated by multi-modal imaging of ICG through mouse tissues *in vivo*. It is shown that optoacoustics consistently provides better sensitivity in differentiating fluorescent targets located at depths beyond 2 mm in turbid tissues, as quantified by evaluating image contrast, signal to noise ratio and spatial resolution performance.

OCIS codes: (110.5120) Photoacoustic imaging; (110.6880) Three-dimensional image acquisition; (170.5120) Photoacoustic imaging; (170.2520) Fluorescence microscopy; (330.1800) Vision - contrast sensitivity.

References and links

1. D. J. Webb and C. M. Brown, "Epi-Fluorescence Microscopy," Methods Mol. Biol. **931**, 29–59 (2012).
2. J. B. Grimm, A. K. Muthusamy, Y. Liang, T. A. Brown, W. C. Lemon, R. Patel, R. Lu, J. J. Macklin, P. J. Keller, N. Ji, and L. D. Lavis, "A general method to fine-tune fluorophores for live-cell and in vivo imaging," Nat. Methods **14**(10), 987–994 (2017).
3. P. J. Cranfill, B. R. Sell, M. A. Baird, J. R. Allen, Z. Lavagnino, H. M. de Gruiter, G. J. Kremers, M. W. Davidson, A. Ustione, and D. W. Piston, "Quantitative assessment of fluorescent proteins," Nat. Methods **13**(7), 557–562 (2016).
4. O. S. Wolfbeis, "An overview of nanoparticles commonly used in fluorescent bioimaging," Chem. Soc. Rev. **44**(14), 4743–4768 (2015).
5. S. J. Sahl, S. W. Hell, and S. Jakobs, "Fluorescence nanoscopy in cell biology," Nat. Rev. Mol. Cell Biol. **18**(11), 685–701 (2017).
6. P. W. Winter, A. G. York, D. D. Nogare, M. Ingaramo, R. Christensen, A. Chitnis, G. H. Patterson, and H. Shroff, "Two-photon instant structured illumination microscopy improves the depth penetration of super-resolution imaging in thick scattering samples," Optica **1**(3), 181–191 (2014).
7. Y. Yamada and S. Okawa, "Diffuse optical tomography: Present status and its future," Opt. Rev. **21**(3), 185–205 (2014).
8. A. T. Eggebrecht, S. L. Ferradal, A. Robichaux-Viehoever, M. S. Hassanpour, H. Dehghani, A. Z. Snyder, T. Hershey, and J. P. Culver, "Mapping distributed brain function and networks with diffuse optical tomography," Nat. Photonics **8**(6), 448–454 (2014).
9. A. Ale, V. Ermolayev, E. Herzog, C. Cohrs, M. H. de Angelis, and V. Ntziachristos, "FMT-XCT: in vivo animal studies with hybrid fluorescence molecular tomography-X-ray computed tomography," Nat. Methods **9**(6), 615–620 (2012).
10. F. Stuker, J. Ripoll, and M. Rudin, "Fluorescence Molecular Tomography: Principles and Potential for Pharmaceutical Research," Pharmaceutics **3**(4), 229–274 (2011).

#315700 https://doi.org/10.1364/BOE.9.002229
Journal © 2018 Received 19 Dec 2017; revised 8 Mar 2018; accepted 9 Mar 2018; published 19 Apr 2018

Biomedical Optics EXPRESS

11. X. L. Deán-Ben, S. Gottschalk, B. Mc Larney, S. Shoham, and D. Razansky, "Advanced optoacoustic methods for multiscale imaging of in vivo dynamics," Chem. Soc. Rev. **46**(8), 2158–2198 (2017).
12. X. L. Deán-Ben, S. Gottschalk, G. Sela, S. Shoham, and D. Razansky, "Functional optoacoustic neuro-tomography of calcium fluxes in adult zebrafish brain in vivo," Opt. Lett. **42**(5), 959–962 (2017).
13. M. R. Tomaszewski, I. Q. Gonzalez, J. P. O'Connor, O. Abeyakoon, G. J. Parker, K. J. Williams, F. J. Gilbert, and S. E. Bohndiek, "Oxygen Enhanced Optoacoustic Tomography (OE-OT) Reveals Vascular Dynamics in Murine Models of Prostate Cancer," Theranostics **7**(11), 2900–2913 (2017).
14. M. T. Berninger, P. Mohajerani, M. Wildgruber, N. Beziere, M. A. Kimm, X. Ma, B. Haller, M. J. Fleming, S. Vogt, M. Anton, A. B. Imhoff, V. Ntziachristos, R. Meier, and T. D. Henning, "Detection of intramyocardially injected DiR-labeled mesenchymal stem cells by optical and optoacoustic tomography," Photoacoustics **6**, 37–47 (2017).
15. P. Subochev, A. Orlova, M. Shirmanova, A. Postnikova, and I. Turchin, "Simultaneous photoacoustic and optically mediated ultrasound microscopy: an in vivo study," Biomed. Opt. Express **6**(2), 631–638 (2015).
16. X. L. Deán-Ben and D. Razansky, "Functional optoacoustic human angiography with handheld video rate three dimensional scanner," Photoacoustics **1**(3-4), 68–73 (2013).
17. Z. Guo, S. Park, J. Yoon, and I. Shin, "Recent progress in the development of near-infrared fluorescent probes for bioimaging applications," Chem. Soc. Rev. **43**(1), 16–29 (2014).
18. D. M. Shcherbakova and V. V. Verkhusha, "Near-infrared fluorescent proteins for multicolor in vivo imaging," Nat. Methods **10**(8), 751–754 (2013).
19. S. M. van den Wildenberg, B. Prevo, and E. J. Peterman, "A brief introduction to single-molecule fluorescence methods," Methods Mol. Biol. **783**, 81–99 (2011).
20. A. M. Winkler, K. Maslov, and L. V. Wang, "Noise-equivalent sensitivity of photoacoustics," J. Biomed. Opt. **18**(9), 097003 (2013).
21. C. J. H. Ho, G. Balasundaram, W. Driessen, R. McLaren, C. L. Wong, U. S. Dinish, A. B. E. Attia, V. Ntziachristos, and M. Olivo, "Multifunctional Photosensitizer-Based Contrast Agents for Photoacoustic Imaging," Sci. Rep. **4**(1), 5342 (2015).
22. M. Seeger, A. Karlas, D. Soliman, J. Pelisek, and V. Ntziachristos, "Multimodal optoacoustic and multiphoton microscopy of human carotid atheroma," Photoacoustics **4**(3), 102–111 (2016).
23. B. Rao, F. Soto, D. Kerschensteiner, and L. V. Wang, "Integrated photoacoustic, confocal, and two-photon microscope," J. Biomed. Opt. **19**(3), 036002 (2014).
24. I. Kosik and J. J. L. Carson, "Combined 3D photoacoustic and 2D fluorescence imaging of indocyanine green contrast agent flow," Proc. SPIE **8581**, 858143 (2013).
25. D. Razansky and V. Ntziachristos, "Hybrid photoacoustic fluorescence molecular tomography using finite-element-based inversion," Med. Phys. **34**(11), 4293–4301 (2007).
26. Z. Chen, X. L. Deán-Ben, S. Gottschalk, and D. Razansky, "Hybrid system for in vivo epifluorescence and 4D optoacoustic imaging," Opt. Lett. **42**(22), 4577–4580 (2017).
27. F. J. O. Landa, X. L. Deán-Ben, R. Sroka, and D. Razansky, "Volumetric Optoacoustic Temperature Mapping in Photothermal Therapy," Sci. Rep. **7**(1), 9695 (2017).
28. M. Goutayer, F. N. Y. Garcia, and I. Texier-Nogues, "Fluorescent emulsion of indocyanine green," (Google Patents, 2016).
29. B. Yuan, N. Chen, and Q. Zhu, "Emission and absorption properties of indocyanine green in Intralipid solution," J. Biomed. Opt. **9**(3), 497–503 (2004).
30. https://www.thermofisher.com/de/de/home/references/molecular-probes-the-handbook/technical-notes-and-product-highlights/the-alexa-fluor-dye-series.html
31. https://www.licor.com/bio/products/reagents/irdye/800cw/
32. S. L. Jacques, "Optical properties of biological tissues: a review," Phys. Med. Biol. **58**(11), R37–R61 (2013).
33. X. L. Deán-Ben, A. Ozbek, and D. Razansky, "Volumetric real-time tracking of peripheral human vasculature with GPU-accelerated three-dimensional optoacoustic tomography," IEEE Trans. Med. Imaging **32**(11), 2050–2055 (2013).
34. A. A. Michelson, Studies in optics (The University of Chicago Press, Chicago, Ill., 1927).
35. Z. Qin, D. J. Hall, M. A. Liss, C. K. Hoh, C. J. Kane, A. M. Wallace, and D. R. Vera, "Optimization via specific fluorescence brightness of a receptor-targeted probe for optical imaging and positron emission tomography of sentinel lymph nodes," J. Biomed. Opt. **18**(10), 101315 (2013).
36. I. Stoffels, S. Morscher, I. Helfrich, U. Hillen, J. Leyh, N. C. Burton, T. C. Sardella, J. Claussen, T. D. Poeppel, H. S. Bachmann, A. Roesch, K. Griewank, D. Schadendorf, M. Gunzer, and J. Klode, "Metastatic status of sentinel lymph nodes in melanoma determined noninvasively with multispectral optoacoustic imaging," Sci. Transl. Med. **7**(317), 317ra199 (2015).
37. X. L. Deán-Ben, D. Razansky, and V. Ntziachristos, "The effects of acoustic attenuation in optoacoustic signals," Phys. Med. Biol. **56**(18), 6129–6148 (2011).
38. O. T. Bruns, T. S. Bischof, D. K. Harris, D. Franke, Y. Shi, L. Riedemann, A. Bartelt, F. B. Jaworski, J. A. Carr, C. J. Rowlands, M. W. B. Wilson, O. Chen, H. Wei, G. W. Hwang, D. M. Montana, I. Coropceanu, O. B. Achorn, J. Kloepper, J. Heeren, P. T. C. So, D. Fukumura, K. F. Jensen, R. K. Jain, and M. G. Bawendi, "Next-generation*in vivo*optical imaging with short-wave infrared quantum dots," Nat Biomed Eng **1**(4), 56 (2017).

Biomedical Optics EXPRESS

39. G. Hong, S. Diao, J. Chang, A. L. Antaris, C. Chen, B. Zhang, S. Zhao, D. N. Atochin, P. L. Huang, K. I. Andreasson, C. J. Kuo, and H. Dai, "Through-skull fluorescence imaging of the brain in a new near-infrared window," Nat. Photonics **8**(9), 723–730 (2014).
40. P. W. Wright, L. M. Brier, A. Q. Bauer, G. A. Baxter, A. W. Kraft, M. D. Reisman, A. R. Bice, A. Z. Snyder, J. M. Lee, and J. P. Culver, "Functional connectivity structure of cortical calcium dynamics in anesthetized and awake mice," PLoS One **12**(10), e0185759 (2017).
41. W. Jahr, B. Schmid, C. Schmied, F. O. Fahrbach, and J. Huisken, "Hyperspectral light sheet microscopy," Nat. Commun. **6**(1), 7990 (2015).
42. R. Cao, J. P. Kilroy, B. Ning, T. Wang, J. A. Hossack, and S. Hu, "Multispectral photoacoustic microscopy based on an optical-acoustic objective," Photoacoustics **3**(2), 55–59 (2015).
43. V. Ermolayev, X. L. Dean-Ben, S. Mandal, V. Ntziachristos, and D. Razansky, "Simultaneous visualization of tumour oxygenation, neovascularization and contrast agent perfusion by real-time three-dimensional optoacoustic tomography," Eur. Radiol. **26**(6), 1843–1851 (2016).
44. E. M. C. Hillman and A. Moore, "All-optical anatomical co-registration for molecular imaging of small animals using dynamic contrast," Nat. Photonics **1**(9), 526–530 (2007).
45. X. L. Deán-Ben, A. C. Stiel, Y. Jiang, V. Ntziachristos, G. G. Westmeyer, and D. Razansky, "Light fluence normalization in turbid tissues via temporally unmixed multispectral optoacoustic tomography," Opt. Lett. **40**(20), 4691–4694 (2015).
46. G. Marriott, S. Mao, T. Sakata, J. Ran, D. K. Jackson, C. Petchprayoon, T. J. Gomez, E. Warp, O. Tulyathan, H. L. Aaron, E. Y. Isacoff, and Y. Yan, "Optical lock-in detection imaging microscopy for contrast-enhanced imaging in living cells," Proc. Natl. Acad. Sci. U.S.A. **105**(46), 17789–17794 (2008).
47. L. Xi, G. Zhou, N. Gao, L. Yang, D. A. Gonzalo, S. J. Hughes, and H. Jiang, "Photoacoustic and fluorescence image-guided surgery using a multifunctional targeted nanoprobe," Ann. Surg. Oncol. **21**(5), 1602–1609 (2014).
48. P. Shao, W. Shi, P. Hajireza, and R. J. Zemp, "Integrated micro-endoscopy system for simultaneous fluorescence and optical-resolution photoacoustic imaging," J. Biomed. Opt. **17**(7), 0760241 (2012).
49. V. Gaind, S. Kularatne, P. S. Low, and K. J. Webb, "Deep-tissue imaging of intramolecular fluorescence resonance energy-transfer parameters," Opt. Lett. **35**(9), 1314–1316 (2010).
50. Y. Wang, J. Xia, and L. V. Wang, "Deep-tissue photoacoustic tomography of Förster resonance energy transfer," J. Biomed. Opt. **18**(10), 101316 (2013).

1. Introduction

Fluorescence (FL) imaging is an essential tool in biomedical research offering superb molecular sensitivity and specificity [1]. An increasing number of FL proteins, organic dyes and other agents are used to provide new insights into gene expression, protein function and other cellular processes non-invasively [2–4]. However, inevitable trade-offs between spatial resolution, penetration depth, temporal resolution and sensitivity are common traits of *in vivo* FL imaging. For instance, microscopic techniques can attain high spatial resolution, which can also be extended beyond the optical diffraction limit [5, 6]. Yet, the small field of view and the shallow imaging depth remain major limitations for these methods. Macroscopic optical imaging employs instead deeply penetrating diffuse photons in the near infrared (NIR) spectrum [7, 8]. Techniques like fluorescence molecular tomography (FMT) have therefore enabled unprecedented capabilities to visualize biological processes at the molecular level in whole mice *in vivo* [9, 10] to the detriment of poor spatial resolution in deep tissue regions.

Optoacoustic (OA) imaging has evolved as a powerful molecular imaging modality owing to the unique combination between high spatio-temporal resolution, large scalability, deep penetration and spectrally-enriched contrast [11]. To date, OA imaging has been widely employed in preclinical and clinical studies in the fields of vascular biology, oncology, neurology or cardiology [12–16], to name a few examples. As opposed to FL imaging, OA techniques readily achieve label-free contrast based on optical absorption of endogenous substances, such as oxy- and deoxy-hemoglobin, melanin, bilirubin, lipids and water [11]. FL substances and other agents that absorb light in visible and near-infrared (NIR) wavelengths further enhance the versatility of the contrast mechanism exploited by the OA imaging, making it particularly advantageous for functional and molecular imaging applications.

FL dyes with absorption in the NIR spectrum represent an excellent choice for contrast-enhanced imaging, in particular when low background and high signal-to-noise ratio (SNR) are of interest. Light in this wavelength range can penetrate deep into tissues, hence tracking of specific biomolecules labelled with NIR dyes becomes possible in small animals at the whole-body level, facilitating progress in basic biological research and drug discovery [17,

Biomedical Optics EXPRESS

18]. FL dyes can provide both FL and OA contrast, thus making it possible to synergistically exploit the advantages of both modalities. While both FL and OA signal intensities are proportional to the extinction coefficient of the dye ε, the FL signal scales with the quantum yield (QY) while the OA signal strength is proportional to 1-QY. Since organic FL dyes with peak absorption in the NIR spectrum usually have a relatively high extinction coefficient (ε) and a relatively low QY, they are highly suitable for both modalities [11].

Combining FL and OA imaging may provide a number of complementary advantages. While FL imaging can reach single molecule sensitivity in superficial microscopic observations [19], measurable OA signals could only be attained in similar experiments from hundreds to thousands of molecules [20]. Yet, OA imaging achieves significantly better spatial resolution in deep tissue observations [11] while it was also found less prone to photobleaching and autofluorescence interference [21]. To this end, several approaches have been suggested for exploiting the complementary advantages of FL and OA imaging [22–25], yet no systematic comparison has been performed regarding their actual performance in detecting fluorescent contrast agents.

In this work, we use a recently-introduced hybrid epifluorescence and volumetric OA system [26] for a comprehensive sensitivity comparison between the two modalities in detecting deep-seated NIR fluorescent agents.

2. Materials and methods

2.1. Hybrid epifluorescence three-dimensional optoacoustic imaging system

The hybrid system is depicted in Fig. 1. A custom-made electron multiplying charge-coupled device (EMCCD)-based fiberscope (Zibra Corporation, USA) was inserted into the cylindrical cavity of a spherical ultrasound array used for OA signal detection. The fiberscope consists of a 1.4 mm diameter optic image guide made of 100000 fibers and an illumination bundle composed of 7 fibers having 600 μm diameter and numerical aperture (NA) of 0.4. An emission filter was placed in front of the EMCCD camera (Andor Luca R, Oxford Instruments, UK) to selectively collect the FL responses transmitted through the optic guide. Considering a working distance of ~37 mm, the FL imaging system has an overall NA of 0.025 in water. The ultrasound array (custom-made by Imasonic SaS, France) used to collect OA signals consists of 512 individual piezocomposite elements with ~2.5 mm diameter, 5 MHz central frequency and ~100% detection bandwidth [27]. The elements are uniformly distributed on a 40 mm radius spherical surface covering an angle of 140° (1.3π solid angle). Light from an optical parametric oscillator (OPO)-based short-pulsed laser (Innolas Laser GmbH, Germany) was guided via the illumination bundle of the fiberscope, simultaneously exciting the OA and FL responses. The illumination spot on the surface of imaged targets had a full-width at half-maximum (FWHM) of ~10mm.

2.2. Imaging of fluorescent dyes

Several common NIR FL dyes were used for the sensitivity comparison, including indocyanine green (ICG, PULSION, Germany) [28, 29], Alexa Fluor 750 (AF750, Invitrogen, USA) [30], Alexa Fluor 750 (AF750, Invitrogen, Eugene, OR, USA) [30] and IRDye 800CW Maleimide (LI-COR, USA) dyes [31] whose main properties are summarized in Table 1.

The FL dyes were injected into a polyethylene tubing having 0.58 mm inner and 0.96 mm outer diameters (Smiths Medical ASD Inc., USA) and immersed inside a tank containing tissue-mimicking medium (Tank 2 in Fig. 1a). The average light absorption and scattering properties of soft biological tissues were mimicked by diluting 33.3% (v/v) of 3.5%-fat milk and 0.1% (v/v) of India ink with 125 OD (Higgins Waterproof Black India Ink, USA) [32]. The imaging probe was then immersed into a smaller water-filled tank (Tank 1 in Fig. 1a) that has a 2 cm opening on its bottom sealed watertight with a thin transparent polyethylene membrane. By vertically moving the small tank inside the larger tank while keeping the

Biomedical Optics EXPRESS

tubing and the center of the spherical detection array in a stationary position, the effective imaging depth of the tubing in the absorbing and scattering medium was varied between 0 and 12 mm with 2 mm steps.

The laser wavelength was tuned to 770 nm to excite ICG and IRDye 800CW, and to 680 nm and 749 nm to excite AF700 and AF750, respectively. The experiment was performed by setting the pulse repetition frequency (PRF) of the laser to 10 Hz. The excitation light fluence at the surface of the tissue-mimicking medium was ~5 mJ/cm^2. For AF700, a long pass filter (Edmund Optics, Stock # 62-980, USA) with 700 nm cut-on wavelength was placed in front of the camera. Similarly, a long pass filter (Edmund Optics, Stock # 66-227, USA) with 800 nm cut-on wavelength was employed for imaging of the ICG, AF750 and IRDye 800CW dyes. The integration time of the EMCCD camera was set to 0.1 s. Both FL and OA signals were averaged over 1 s, corresponding to 10 FL and OA frames. Volumetric OA image reconstruction was performed with a GPU-accelerated 3D back-projection method [33]. Cross-sectional slices corresponding to the depth of the tubing were extracted from the volumetric OA data at the tubing location in order to enable proper comparison with the planar FL recordings. Imaging performance of both imaging modalities as a function of depth was first compared in terms of image contrast calculated via

$$C = (I_{sig} - I_{bg}) / (I_{sig} + I_{bg}), \quad (1)$$

where I_{sig} and I_{bg} are the mean pixel values of selected regions of interest (ROIs) in the target and in the background, respectively [34]. The depth-dependent resolution was estimated as the FWHM of the central profile perpendicular to the tubing.

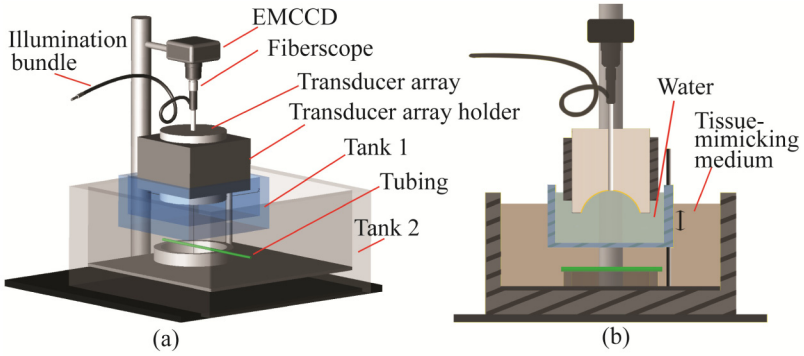

Fig. 1. Lay-out of the hybrid fluorescence-optoacoustic experimental set-up used for the sensitivity comparison. (a) Three-dimensional lay-out of the set-up; (b) Cross sectional view of (a). Tank 1 was filled with a tissue mimicking medium. Tank 2 was filled with distilled water to couple the acoustic signal from the tubing to the transducer array. During the experiment, only the water tank was translated up and down to change the depth of the tubing within the tissue-mimicking medium.

Table 1. Dye information of ICG [28, 29], AF700 [30], AF750 [30], and IRDye 800CW [31, 35].

Dye	Molecular weight [g/mol]	Abs./Em. Max [nm]	Quantum yield[a] (QY)	Extinction coef. [b] (ε) [cm^{-1}M^{-1}]	Fluorescence ∝ QY*ε [cm^{-1}M^{-1}]	OA ∝ (1-QY)*ε [cm^{-1}M^{-1}]
ICG	775	777/802	0.042	204,000	8,568	195,432
AF750	~1300	749/775	0.12	290,000	34,800	255,200
AF700	~1400	702/723	0.25	205,000	51,250	153,750
IRDye 800CW	1091.1	774/789	0.12	240,000	28,800	211,200

[a] QY measurements were made in PBS. The data was taken either from the dye manufacturer or published literature. [b] Extinction coefficients were extracted from the information provided by the dye manufacturers.

Biomedical Optics EXPRESS

2.3. In vivo *mouse experiment*

The sensitivity performance of the hybrid system for epifluorescence and OA modes was further experimentally tested *in vivo*. For this, a 99 days old athymic nude mouse (Hsd:Athymic Nude-Foxn1^{nu}, obtained from Envigo, Netherlands) was anesthetized with ~2% Isoflurane in pure oxygen (v/v) supplied at a flow rate of 0.8 L/min. The same tubing used in the phantom experiment was placed under the right hind leg of the mouse and covered with ultrasound gel. The water tank (Tank 1) was then placed on top of the mouse leg to couple the acoustic signal into the detection array. Tank 2 was not necessary for the *in vivo* experiments. Animal handling procedures were performed according to the directives on animal experimentation of the Helmholtz Center Munich and with approval from the Government District of Upper Bavaria. The tubing was filled with ICG at concentrations of 2 µg/ml and 20 µg/ml. The OPO laser was tuned to 715 nm excitation wavelength and the PRF was set to 10 Hz. For FL imaging, the long-pass filter with 750 nm cut-on wavelength was employed. The fluorescence camera was synchronized with the laser pulses and the exposure time was set to 0.1 s. Both OA and FL images were averaged for 1 s, i.e., 10 frames.

3. Results

Figure 2 displays results of the imaging performance comparison in phantoms. Specifically, the epifluorescence (Fig. 2(a)) and cross-sectional OA (Fig. 2(b)) images of the tubing embedded in the tissue-mimicking medium are shown for ICG concentrations of 10 µg/ml and 50 µg/ml. All images were normalized to their respective maximum value. As expected, significant degradation of image contrast and spatial resolution performance with depth was observed in the FL mode with the tubing becoming unresolvable beyond 2 mm depth in the turbid medium. On the contrary, no resolution degradation was perceived in the OA images with the dye-filled tubing clearly resolved at 10 mm depth and beyond, depending on the dye concentration. A quantitative comparison was further performed by calculating the image contrast via Eq. (1) and the image resolution as the FWHM along the normal direction to the tubing. The target and background ROIs employed to calculate image contrast are indicated by the blue boxes in Figs. 2(a) and 2(b). The values obtained as a function of target concentration and depth are further shown in Fig. 2(c), in good accordance with the qualitative perception in the images displayed. The calculated values of the FWHM, representing the measured diameter of the tubing in the epifluorescence and cross-sectional OA images, are plotted in Fig. 2(d). Note that the low image SNR precluded reliable calculation of the FWHM beyond certain target depths. When placed at the surface of tissue-mimicking medium (i.e., 0 mm depth), the calculated FWHM was 0.91 mm for the FL and 0.96 mm for the OA mode. These values are close to the outer diameter of the tubing, even though the ICG volume is confined to the inner diameter. We ascribe this discrepancy to optical scattering and acoustic distortion in the tubing material. As the target depth increases, the measured diameter of the tubing increases significantly in the FL images while remaining nearly constant in the OA images. In fact, tubing location and shape become unrecognizable in the FL mode when embedded at depths beyond 2 mm in the tissue-mimicking medium. Such loss of contrast and resolution effectively limits the capability to identify FL substances within a light-scattering biological sample.

Biomedical Optics EXPRESS

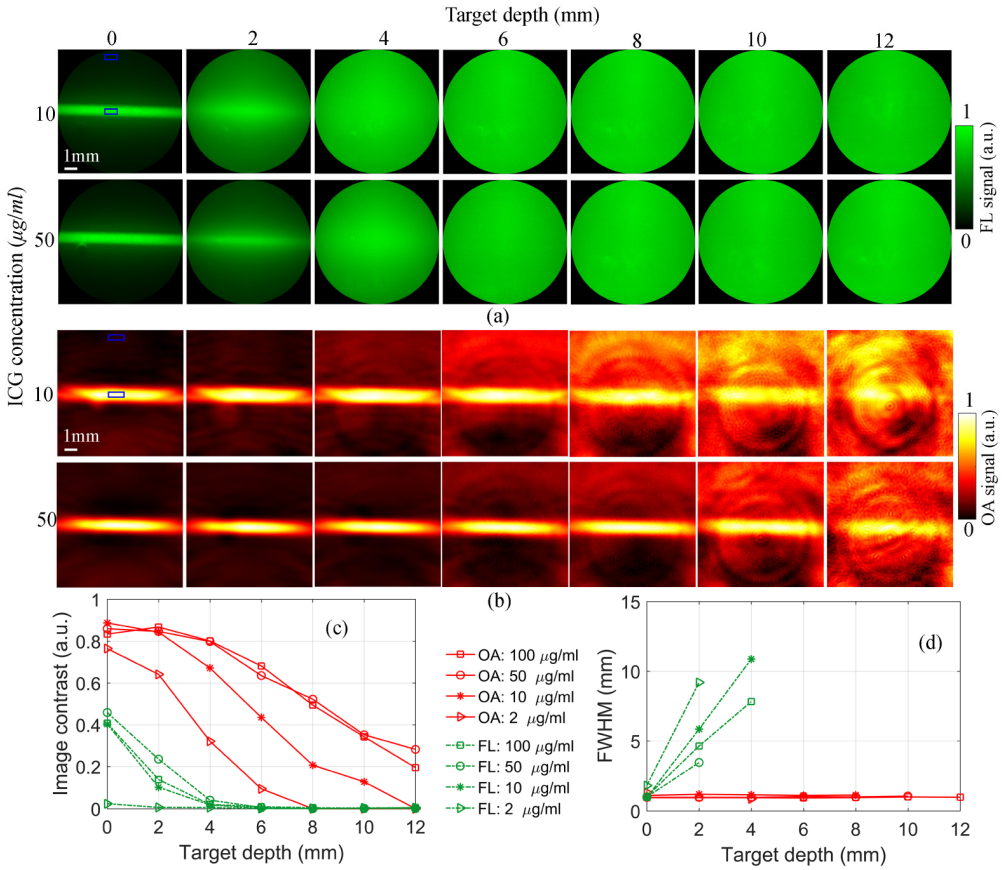

Fig. 2. Experimental imaging results for the ICG-filled tubing. (a) Fluorescence images captured at different target depths with ICG concentration of 10 μg/ml and 50 μg/ml. Note that each image is normalized to its own maximum value to optimize the contrast. (b) The corresponding optoacoustic single slice images extracted from the reconstructed volumetric image data. Both fluorescence and optoacoustic images were averaged over 1 s acquisitions. (c) Plot of image contrast which was calculated based on the ROIs shown in (a) and (b). (d) FWHM of the tubing diameter extracted from the images in (a) and (b).

Figure 3 displays the image contrast and FWHM as a function of depth for the other FL dyes analyzed, i.e., AF700, AF750 and IRDye 800CW. Figures 3(a) and 3(b) show the results for the tubing filled with AF700. The high QY of AF700 at its 680 nm excitation wavelength caused FL signal saturation for a concentration of 50 μg/ml at 0 and 2 mm depths and for a 20 μg/ml concentration at 0 mm depth. The strong light scattering at 680nm also made the tubes unresolvable in the FL mode at depths beyond 6 mm. On the other hand, it was not possible to optoacoustically visualize AF700 at 5 μg/ml concentration for any depth due to low SNR of the reconstructed images. Figures 3(c) and 3(d) show the corresponding results for the tubing filled with AF750. The smaller QY and larger molar extinction coefficient of AF750 with respect to AF700 (Table 1) results in much better OA image contrast, making it superior to that of FL even for relatively shallow depths. On the other hand, the longer excitation and emission wavelength of AF750 contributes to reduced light scattering making the dye resolvable also beyond 6 mm depths. Figures 3(e) and 3(f) show the results for the tubing filled with IRDye 800CW dye. In general, its performance in terms of image contrast and resolution was found similar to AF750, which is expected since both dyes have similar extinction coefficient and peak excitation wavelength. Note that the QY of IRDye 800CW is

Biomedical Optics EXPRESS

not available from the manufacturer, although it was previously reported to be similar to that of AF750 [35].

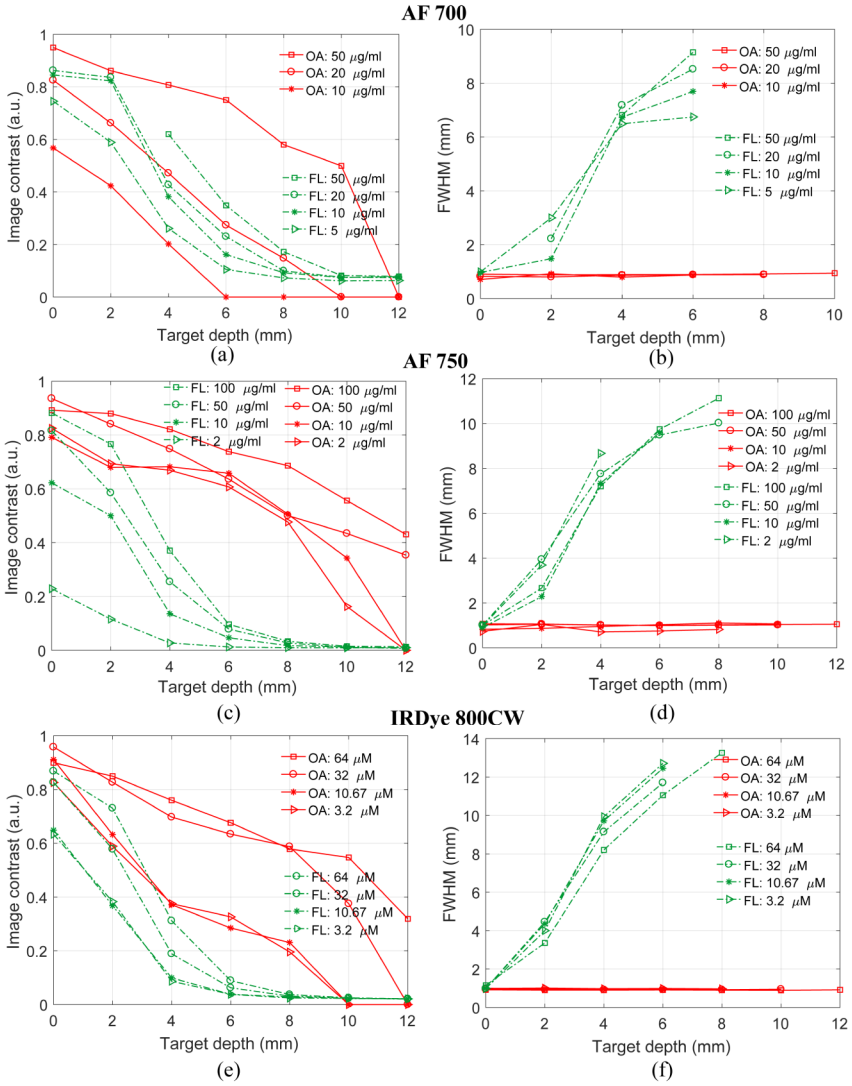

Fig. 3. Image performance comparison for Alexa Fluor 700, Alexa Fluor 750 and IRDye 800CW fluorescent dyes. The left column shows the comparison of image contrast and the right column shows the corresponding FWHM of the tubing extracted from the images. The image contrast was calculated according to the ROIs shown in Figs. 2(a) and 2(b).

Figure 4 shows results of the *in vivo* mouse experiment with the red box in Fig. 4(a) indicating the imaged ROI. Figure 4(b) shows the FL image for an ICG concentration of 20 µg/ml. Note that the bright green part of the tubing was not covered by the mouse leg, so the signal from this particular area effectively corresponds to the reference FL signal for a depth of 0 mm. Figure 4(c) shows the normalized FL image within a smaller ROI covered by the mouse leg, as indicated by the yellow dashed box in Fig. 4(b). Figure 4(d) shows the maximum intensity projection (MIP) of the reconstructed 3D OA image along the depth direction for the same ICG concentration. One may note that the tubing generates stronger OA responses as compared to the mouse tissues. Figure 4(e) shows a single slice OA image approximately at the center of the tubing. Four ROIs indicated by the red boxes in Fig. 4(b)

Biomedical Optics EXPRESS

were selected for quantitative imaging performance analysis. ROI1 corresponds to a depth of 0 mm (not covered by the mouse leg), while ROI2 to ROI4 represent different imaging depths from 2.4 mm to 4.4 mm. Similarly to the phantom imaging results shown in Figs. 2 and 3, the tubing becomes unresolvable by the FL modality already at 2.4 mm depth (ROI2). For the in *vivo* experiments, we further characterized detection sensitivity by calculating the signal-to-noise according to $SNR = 10\log(\mu/\sigma)$ [dB], where μ is the mean pixel value of each ROI and σ is the standard deviation of noise (system noise floor). The latter was calculated from images taken prior to ICG injection in ROI5 containing only water (Fig. 4(b)). Figure 4(f) shows the SNR plots for the FL and OA images for two different ICG concentrations. While the SNR is comparable for both FL and OA cases at 0 mm target depth, it degrades more rapidly with depth in FL images, owing to the double light propagation distance for the FL excitation and emission paths.

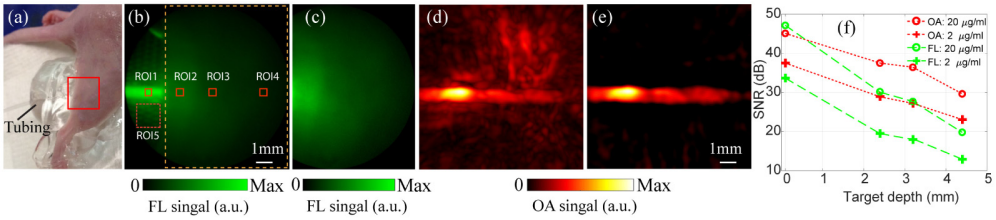

Fig. 4. *In vivo* mouse imaging results. (a) Photograph of the experiment with the tubing placed under the mouse leg. The red box shows the imaged region. (b) Fluorescence image of the tubing containing ICG at 20 μg/ml concentration. (c) Zoom-in fluorescence image from a smaller ROI indicated by the dashed box in (b). (d) The corresponding maximum intensity projection (MIP) of the 3D optoacoustic image acquired from the same area as in (b). (e) Single slice optoacoustic image of the tubing. (f) SNR plots of fluorescence and optoacoustic image intensity for the ROIs shown in (b). The standard deviation of the noise was calculated in ROI5 containing only water.

4. Discussion and conclusions

In this work, image contrast and resolution of FL and OA images were measured for a thin tubing target containing several commonly-used fluorescent contrast agents, which was immersed at different depths within a tissue-mimicking medium. It was shown that FL image contrast and resolution rapidly degrade with depth. In particular, it was challenging to resolve contrast agents beyond ~2 mm depth whereas their unambiguous detection by the FL modality was not possible beyond ~6 mm depth. Conversely, it was possible to resolve the tubing with high contrast and resolution in the OA images when visualizing dye concentrations in the order of 10 μM at depths beyond 10 mm. The results were further corroborated by *in vivo* measurements of ICG taken through living mouse tissues, revealing stronger attenuation of the FL signal and superior contrast, resolution and signal to noise of the OA images at target depths greater than 2 mm. Indeed, it was recently reported that ICG could be detected in clinical OA measurements of human lymph nodes at depths exceeding 20 mm *in vivo* [36], which is generally not feasible with FL imaging without applying invasive procedures. These findings are generally justified when considering that scattering and attenuation are insignificant in the acoustic propagation path for ultrasound frequencies in the low MHz range and propagation distances of up to several centimeters [37].

It was shown that the FWHM of the tubing in the FL images could be accurately measured at greater depth for AF750, ICG and IRDye800 as compared to AF700. This is attributed to the reduced optical scattering at the longer excitation and emission wavelengths. Recently, the availability of InGaAs cameras has fostered the development of FL imaging approaches in the second NIR window [38, 39], where the resolving capacity of FL imaging in deeper regions is expected to be enhanced due to the reduced photon scattering.

Biomedical Optics EXPRESS

A number of aspects of our comparative imaging performance and sensitivity study may need further clarification. In general, sensitivity of an imaging system can be interpreted as its capability to detect and/or resolve the presence of a given substance within a biological organism. The present study has employed state-of-the-art instrumentation and imaging configurations that are commonplace in recently reported *in vivo* investigations [12, 36, 40], both from the OA and FL imaging perspectives. In particular, highly sensitive matrix detection array and low-noise electronics were used for the OA signal acquisition. Similarly, the epifluorescence system contained a highly-sensitive cooled EMCCD camera and used an optical system with NA of 0.025, commonplace in macroscopic planar FL setups. Yet, detection sensitivity may vary depending on the technologies employed for the light and ultrasound detection as well as signal unmixing and background rejection strategies used in each particular system. For instance, the autofluorescence generated by endogenous substances in biological tissues can be minimized in the NIR spectrum [39], especially when imaging in the second NIR window [38]. Furthermore, endogenous absorbers, particularly blood, generate a strong background OA signal [11], which can be similarly minimized by moving into longer NIR wavelengths. Better differentiation of signals over the background can also be achieved by tracking changes in the spectral or temporal domains. For instance, multispectral unmixing can be used to identify specific absorption or emission spectra of agents [41, 42]. Unspecific signal background can be alternatively rejected by comparing the images taken at different time points, e.g. before, after or during administration of the contrast agent [43, 44]. Temporal unmixing can also be used for a more sensitive differentiation of genetically-expressed photoswitchable fluorescent agents [45, 46]. The hybrid OA-epifluorescence imaging system used in this work provides simultaneous dynamic imaging capabilities with both modalities and further enables fast wavelength-tuning of the excitation wavelength. Thereby, dynamic signal enhancement strategies in the spectral and temporal dimensions can further be exploited to enhance the sensitivity for contrast agent detection.

All in all, it is believed that efficient hybridization between OA and FL has great potential for preclinical research and clinical translation. To this end, a number of studies have reported multimodal or hybrid measurements with FL and OA. Image-guided surgery using a multifunctional targeted nanoprobe in mice was reported with OA imaging providing deep 3D information while FL facilitating detection of residual cancerous cells in the surgical cavity [47]. OA tomography images were also used for improving accuracy of fluorescence molecular tomography reconstructions [25]. An integrated system combining label-free optoacoustic microscopy with fluorescence micro-endoscopy was used to visualize fluorescently-labeled cellular components and optically absorbing microvasculature simultaneously [48]. Other potential implementations include imaging of Förster resonance energy transfer (FRET) in both OA and FL modes in order to extend the powerful capacity of FRET for detecting nucleic acid hybridization and transport of lipids into deeper tissues [49, 50].

In conclusion, a systematic comparison of the depth-dependent imaging performance of epifluorescence versus OA imaging was performed in this study using a hybrid imaging system and several commonly used NIR dyes. It was found that optoacoustics provides better sensitivity in differentiating fluorescent targets located at depths beyond 2 mm in turbid tissues, as quantified by evaluating the metrics of image contrast, signal to noise ratio and spatial resolution performance Despite the better performance of optoacoustics in deep tissue imaging, its synergistic combination and simultaneous cross-validation with epifluorescence imaging can greatly benefit numerous studies looking at rapid *in vivo* dynamics, such as neural activity, organ perfusion, circulation of cells or contrast agent uptake.

Biomedical Optics EXPRESS

Funding

European Research Council (ERC-2015-CoG-682379); US National Institute of Health (R21-EY026382); Human Frontier Science Program (RGY0070/2016) and Deutsche Forschungsgemeinschaft (RA1848/5-1).

Acknowledgments

The authors would like to thank M. Reiss for the assistance in animal experimentation.

Disclosures

The authors declare no competing financial interests.